Astronomy & Astrophysics manuscript no. aanda
November 11, 2025

Not all protoclusters host evolved galaxies: Evidence for reduced environmental effects in a lower halo mass protocluster at $z = 7.66$

Callum Witten[1], Pascal A. Oesch[1,2,3], Jake S. Bennett[4], Romain A. Meyer[1], Emma Giovinazzo[1], Alba Covelo-Paz[1], William M. Baker[5], and Lucy R. Ivey[6,7]

[1] Department of Astronomy, University of Geneva, Chemin Pegasi 51, 1290 Versoix, Switzerland
[2] Cosmic Dawn Center (DAWN), Copenhagen, Denmark
[3] Niels Bohr Institute, University of Copenhagen, Jagtvej 128, 2200 Copenhagen, Denmark
[4] Center for Astrophysics | Harvard & Smithsonian, 60 Garden Street, Cambridge, MA 02138, USA
[5] DARK, Niels Bohr Institute, University of Copenhagen, Jagtvej 155A, DK-2200 Copenhagen, Denmark
[6] Kavli Institute for Cosmology, University of Cambridge, Madingley Road, Cambridge, CB3 0HA, UK
[7] Cavendish Laboratory, University of Cambridge, 19 JJ Thomson Avenue, Cambridge CB3 0HE, UK
e-mail: `callum.witten@unige.ch`

ABSTRACT

The progenitors of present-day galaxy clusters offer crucial insight into how galaxies and large-scale structure co-evolve in the early Universe. We present *JWST*/NIRCam grism spectroscopy of the photometrically identified $z = 7.66$ protocluster core in the SMACS J0723.3-7327 lensing field, SMACS-PC-z7p7. Six [O III]-emitters and five additional photometric candidates are found within a 0.3 arcmin^2 (1.5 cMpc^2) region, corresponding to an overdensity of $\delta \sim 200$. Despite the extreme overdensity, the resident galaxies exhibit star-formation histories, UV-slopes and neutral hydrogen column densities that are consistent with those of field galaxies at similar redshifts. This is in stark contrast with the consistently high neutral hydrogen column densities, old stellar populations and large dust masses of galaxies within a $z = 7.88$ protocluster in the Abell 2744 field. Comparison with the TNG-Cluster and TNG300 simulations indicates a halo mass of $\log_{10}(M_{200c}[M_\odot]) = 11.4 \pm 0.2$, and implies that, on average, SMACS-PC-z7p7 will evolve into a present-day Fornax-like cluster ($\log_{10}(M_{200c,\,z=0}[M_\odot]) = 13.7 \pm 0.6$). The uniformly young, highly star-forming nature of the galaxy population of SMACS-PC-z7p7 suggests that environmental effects only become significant above halo masses of $\log_{10}(M_{200c}[M_\odot]) \gtrsim 11.5$. Comparison to other $z \gtrsim 7$ protoclusters reveals that vigorous star formation persists in lower-mass protoclusters, whereas accelerated evolution and suppression of star formation emerge in more massive haloes. SMACS-PC-z7p7 therefore represents an early stage of protocluster assembly, where residence within an overdense environment still enhances star formation, and feedback processes have yet to exert a significant influence.

Key words. galaxies: high-redshift – galaxies: evolution – galaxies: clusters: general – dark ages, reionization, first stars – large-scale structure of Universe

. Introduction

n the Λ cold dark matter (ΛCDM; Peebles 1982; Blumenhal et al. 1984) model of the Universe, the dark matter (DM) istribution is inhomogeneous on small scales. While baryonic matter falls onto early DM haloes, forming the first stars and alaxies, on larger scales ($\sim 0.1 - 1$ pMpc) DM overdensiies result in loose clusters of galaxies. With cosmic time, these lusters become virialised and at a transitional DM halo mass ($\log_{10}(M_{\rm Halo}\ [M_\odot]) \sim 11.8$; Dekel & Birnboim 2006), infalling gas is shock-heated. The ensuing hot halo that constitutes the volume-filling phase of the circumgalactic medium (CGM), suppresses star formation in cluster-resident galaxies. At higher redshifts ($z > 1.5$), dense, cold streams can penetrate through the hot halo and support star formation (Katz et al. 2003; Keres et al. 2005; Mandelker et al. 2016; Bennett & Sijacki 2020). Therefore, the progenitors of current-day clusters are expected to be identified as highly star-forming (up to 50% of the cosmic star-formation rate density), dense (on scales of 100 pkpc) collections of galaxies (Behroozi et al. 2013; Chiang et al. 2017; Yajima et al. 2021; Lim et al. 2024; Morokuma-Matsui et al. 2025; Baxter et al. 2025).

These extremely dense regions of the very early Universe are crucial both in terms of early galaxy evolution (Laporte et al. 2017; Harikane et al. 2019; Hashimoto et al. 2023; Arribas et al. 2024; Morishita et al. 2025; Baker et al. 2025; Witten et al. 2025a,b; Li et al. 2025b) and the reionisation process (Laporte et al. 2022; Witstok et al. 2024; Li et al. 2025a). The massive haloes within which these clusters of galaxies reside represent the most extreme nodes of the cosmic web. These are fed by vast filamentary structures, resulting in protocluster resident galaxies that often show excessive damping from dense neutral hydrogen ($N_{\rm HI} > 10^{22}$ cm^{-2}; Li et al. 2025a; Witten et al. 2025b). This gas accretion can drive enhanced and prolonged star formation, which, together with the early formation times of protocluster galaxies, leads to the accelerated evolution of galaxies resident in these dense environments (Thomas et al. 2005). Protocluster-resident galaxies have been found to have increased metallicities, higher dust contents and older stellar populations relative to field galaxies (Laporte et al. 2017; Arribas et al. 2024; Witten et al. 2025a; Li et al. 2025b; Helton et al. 2024a). However, while some protocluster resident galaxies show extreme, evolved properties that are atypical compared to the general high-redshift galaxy population (e.g. Roberts-Borsani et al.

2024), this is not ubiquitous across high-redshift protoclusters (Laporte et al. 2022; Li et al. 2025a; Fudamoto et al. 2025a). The wide variety in the properties of protocluster-resident galaxies demonstrates varying levels of impact from environmental effects. In order to understand what drives these variations, it is crucial to identify and characterise a larger sample of protoclusters, across a diversity of environments and redshifts.

In the era of *JWST*, with its deep imaging and spectroscopic abilities, discoveries of high-redshift overdense environments have been plentiful. These range from those serendipitously discovered in NIRCam imaging or wide-field slitless spectroscopy (Fudamoto et al. 2025a; Castellano et al. 2023; Helton et al. 2024a,b) to those found in targeted searches around objects that are thought to be ideal tracers of massive DM haloes, including quasars (e.g. Kashino et al. 2023; Meyer et al. 2024; Wang et al. 2024b; Pudoka et al. 2024, 2025; Champagne et al. 2025); Lyman-α emitters (Witstok et al. 2024), massive dusty galaxies (Arribas et al. 2024) and UV-bright galaxies (Laporte et al. 2022; Hashimoto et al. 2023; Morishita et al. 2023; Tacchella et al. 2023a; Scholtz et al. 2024). In particular, UV-bright galaxies will become crucial signposts of overdense environments as we move towards wide area, relatively shallow imaging from instruments such as the *Euclid* and *Roman* space telescopes that can detect these rarest UV-bright objects. One of the most promising candidate protoclusters is the environment around two UV-bright galaxies in the SMACS J0723.3-7327 (hereafter SMACS0723) field at $z = 7.66$ (Laporte et al. 2022).

In this paper, we utilise new NIRCam imaging and grism observations around this candidate protocluster, described in Section 2, to build a spectroscopic and photometric sample of protocluster-resident galaxies in Section 3. With our sample in hand, we perform spectral energy distribution (SED)-fitting to establish the properties of resident galaxies in Section 4. We utilise the TNG-Cluster and TNG300 simulations to estimate the virial mass of this protocluster and its projected current-day virial mass in Section 5. In Section 6, we establish a connection between the virial masses of high-redshift protoclusters and the impact of environmental effects, and finally, in Section 7, we report our conclusions.

All of the properties reported throughout this paper, unless otherwise stated, are corrected for lensing using the magnification factor estimated from Pascale et al. (2022).

2. Data

The SMACS0723 field was the subject of the first *JWST* deep field as part of the Early Release Observations (ERO; ID: 2736, Pontoppidan et al. 2022), including Near Infrared Spectrograph (NIRSpec), Near Infrared Camera (NIRCam) and Near Infrared Imager and Slitless Spectrograph (NIRISS) observations. NIRCam observations with the F090W, F150W, F200W, F277W, F356W and F444W filters revealed a number of high-redshift ($z > 7$) photometric candidate galaxies (Morishita & Stiavelli 2023; Donnan et al. 2023; Atek et al. 2023; Adams et al. 2023; Harikane et al. 2023), while NIRSpec observations with the disperser-filter combinations G235M/F170LP and G395M/F290LP spectroscopically confirmed a small sample of such objects (Curti et al. 2023; Brinchmann 2023; Tacchella et al. 2022; Carnall et al. 2023; Trump et al. 2023). The original ERO spectroscopy and imaging of two $z = 7.66$ galaxies suggest they have typical metallicities given their stellar masses (Curti et al. 2023), are young with rising star-formation histories (SFHs) and clumpy morphologies (Tacchella et al. 2023b), and may host active galactic nuclei (AGN, Brinchmann 2023) which drive subsequently detected outflows (Ivey et al. 2025). These two UV-bright ($M_{\rm UV} \sim -20$) galaxies are separated by less than 50 pkpc (see PW4 and PW5 in Figure 1), leading to the hypothesis that they likely reside within a massive dark matter halo. Further supported by an overdensity of photometrically identified galaxies, this region of the SMACS0723 field appears to be a protocluster core candidate at $z = 7.66$ (Laporte et al. 2022), hereafter SMACS-PC-z7p7.

The Build-Up of Large-Scale Structure in the Early Universe Cycle 2 GO program (ID: 4043, PI: Witten) was aimed at spectroscopically confirming the photometric protocluster, SMACS-PC-z7p7. The program utilises simultaneous NIRCam wide-field slitless spectroscopy (WFSS), using the F444W filter, and complementary short-wavelength imaging in the F090W and F115W filters. These observations were conducted with both the R and C grism directions to break the spatial-spectral degeneracy of WFSS and to provide a second dispersal direction for when the spectrum is heavily contaminated (e.g. Naidu et al. 2024). This contamination is especially common when dispersing through the foreground cluster region. The programs primary aims were to detect [O III]-emitters at $z = 7.66$, within SMACS-PC-z7p7, and improve the photometric redshifts of candidate galaxies. Covering a single NIRCam pointing, the 15890 s integration time in each grism direction makes this program among the deepest *JWST* grism observations yet performed.

The simultaneous short-wavelength NIRCam imaging in F115W covers a wavelength range ($1.3 \lesssim \lambda \lesssim 1.7$) that was previously poorly constrained by existing, relatively shallow, *Hubble* Space Telescope imaging and was not included in the ERO filter configuration. This wavelength range is crucial in estimating the redshift of $7 < z < 9$ photometric-candidate galaxies, and as such, there is a significant overlap between the $z \sim 9$ photometric candidates in the literature (e.g. Donnan et al. 2023) and our now spectroscopically confirmed $z = 7.66$ galaxies.

Throughout this paper we use the NIRCam imaging data reductions from the Dawn *JWST* Archive (DJA) [1]. The DJA retrieves level-2 calibrated NIRCam exposures and processes them using the `grizli` software package (Brammer 2019) to derive combined, drizzled images that are aligned to Gaia astrometry. For further information see Valentino et al. (2023). The NIRCam grism data is processed in the same way using the `grizli`[2] code, with standard calibrations but with grism configuration files (V9) provided by Nor Pirzkal[3]. We then follow the same procedure as outlined, e.g., in Oesch et al. (2023) and Meyer et al. (2024), to extract continuum-subtracted, median-filtered grism spectra.

3. Protocluster-resident sample

Given the newly available NIRCam wide-field slitless spectroscopy, we primarily target emission-line galaxies. We begin with a liberal selection criterion, F090W - F115W > 1.5, that is consistent with a Lyman-α break at $z \sim 7$ along with both non-detection at 3σ depth in F090W and a detection at greater than 3σ in F444W. We choose this liberal $z \sim 7$ selection criteria as there exist regions of the SMACS0723 field that are newly imaged by this program and hence only have F090W, F115W and F444W imaging, and thus a selection using only these filters is important.

This selection results in a sample of ~ 2600 objects that require visual inspection. We utilise the `specvizitor` graphi-

[1] https://dawn-cph.github.io/dja/
[2] https://github.com/gbrammer/grizli
[3] https://github.com/npirzkal/GRISMCONF

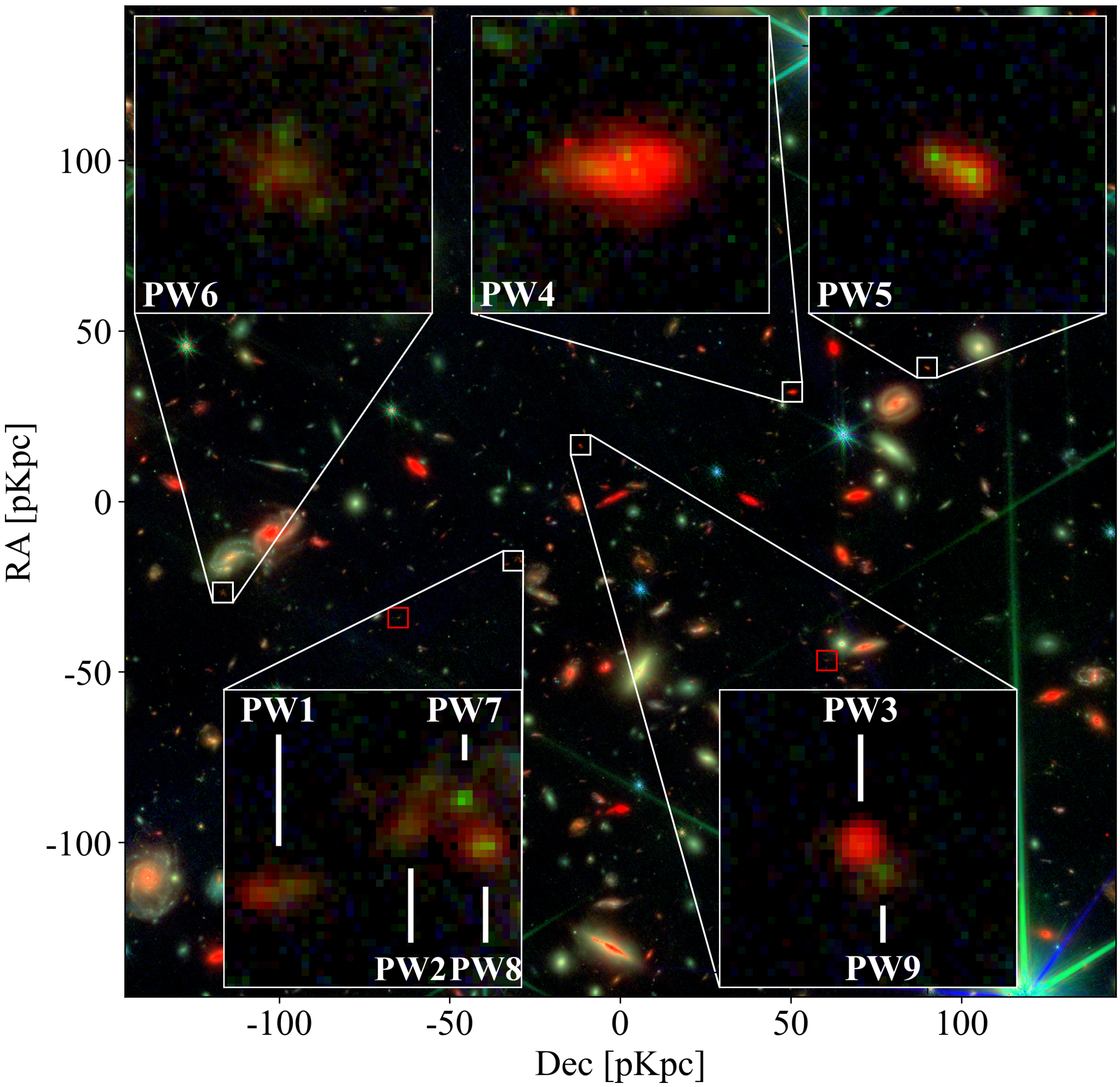

Fig. 1. RGB image using the F090W, F115W and F444W filters, showing the protocluster region in the SMACS0723 field. The inset panels zoom on regions that contain spectroscopically confirmed $z = 7.66$ galaxies. Within the inset panels ($\sim 5 \times 5$ pkpc^2) the names correspond to the galaxies indicated by the markers. The red boxes indicate our two lower confidence photometric candidates. The axes have been corrected for lensing by taking the median magnification, $\mu = 1.43$.

Table 1. The properties of our sample of SMACS-PC-z7p7-resident galaxies. Split into a spectroscopic sample, a high-confidence photometric candidate sample and a sample of photometric candidates that require future confirmation.

ID	RA	Dec.	z_{spec}	M_{UV}	β	$\log(M_\star[M_\odot])$	N_{HI}	μ
PW1	110.86717	-73.43894	7.6653	-18.6 ± 0.2	-1.8 ± 0.3	$8.6^{+0.2}_{-0.2}$	23.0 ± 0.3	1.47
PW3	110.86132	-73.43627	7.6698	-17.9 ± 0.2	-1.4 ± 0.2	NA	< 21.5	1.40
PW4	110.84460	-73.43508	7.6661	-20.36 ± 0.04	-1.4 ± 0.1	$920^{+0.2}_{-0.2}$	< 21.5	1.38
PW5	110.83397	-73.43454	7.6624	-19.95 ± 0.04	-2.1 ± 0.1	$8.1^{+0.2}_{-0.1}$	< 21.5	1.39
PW6	110.88945	-73.43958	7.6625	-19.72 ± 0.03	NA	$8.7^{+0.2}_{-0.2}$	< 21.5	1.43
PW8	110.86599	-73.43887	7.6616	-18.79 ± 0.09	-2.1 ± 0.2	$7.9^{+0.2}_{-0.3}$	< 21.5	1.47
PW2	110.86638	-73.43884	*7.66*	-17.8 ± 0.2	-1.8 ± 0.3	$8.4^{+0.3}_{-0.4}$	< 21.5	1.47
PW7	110.86610	-73.43880	*7.66*	-18.5 ± 0.1	-2.1 ± 0.2	$8.3^{+0.2}_{-0.3}$	< 21.5	1.47
PW9	110.86118	-73.4363	*7.66*	-17.8 ± 0.2	-1.8 ± 0.4	$8.1^{+0.3}_{-0.6}$	< 21.5	1.40
PW12	110.84191	-73.44109	$8.1^{+0.2}_{-0.4}$	-18.6 ± 0.1	-1.9 ± 0.2	$8.1^{+0.3}_{-0.2}$	< 21.5	1.62
PW13	110.87559	-73.44013	$7.4^{+0.3}_{-0.1}$	-18.8 ± 0.2	-2.2 ± 0.3	$8.6^{+0.1}_{-0.2}$	< 21.5	1.49

Notes: Magnification factor from Pascale et al. (2022).

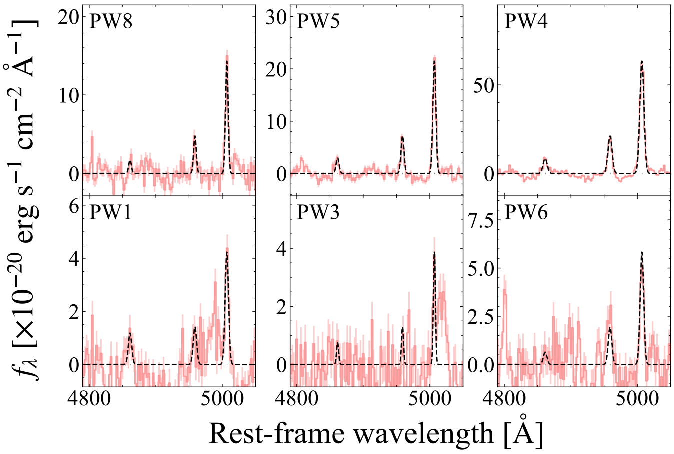

Fig. 2. The rest-frame spectra of [O III]-emitters identified in the SMACS0723 field at $z = 7.66$. Each panel shows a different galaxy, identified by the text in the top left of each panel. The shaded red region around the red solid line shows the error of each spectrum. The dashed line shows the best-fit model spectrum of the Hβ , [O III] λ4960Å and [O III] λ5008Å emission lines. Despite the relative weakness of the emission lines seen from PW3 and PW1, their detection in the 2D spectra in both R and C directions, combined with their consistent photometric redshift, leads us to conclude that they are indeed emission lines at $z = 7.66$.

cal user interface[4] to inspect potential [O III] emitting galaxies at $z \sim 7.66$, and identify a total of six spectroscopically confirmed galaxies. We fit their [O III] and Hβ emission lines with Gaussian profiles and Monte Carlo error propagation, and obtain the fluxes reported in Table A.1 and the redshifts reported in Table 1. The combined spectrum from the R and C grism directions, as well as our best-fit emission line model can be seen in Figure 2 for each galaxy. We note that while the emission line detections for PW3 and PW1 appear to be tentative in the combined 1D spectra, they do appear to be significant based on our emission line modelling, they appear present in both the R and C 2D spectra, and they have SEDs that are consistent with a Lyman-α break at $z \sim 8$. Therefore, we consider these galaxies as spectroscopically confirmed.

We calculate the photometry of each galaxy using the same routine as described in Witten et al. (2025b). We utilise the `Photutils` package (Bradley et al. 2025) with custom apertures and local background subtraction to avoid contamination from the intracluster-light of the foreground cluster (the photometry of each galaxy is reported in Table A.2).

We also search for potential photometric candidates in the immediate environment of our spectroscopic sample. We identify three galaxies, PW2, PW7 and PW9, that are resident within 2 pkpc of a spectroscopically confirmed galaxy, and have a photometric redshift consistent with $z = 7.66$. We consider these as part of our high-confidence protocluster-resident sample. Finally, we utilise the `Eazy` (Brammer et al. 2008) photometric redshift catalogue, released on the DJA[5], to search for further photometric candidates. We identify two robust high-redshift candidates that also have `Eazy` photometric redshifts consistent with $z = 7.66$ (See Table 1). However, the lack of medium band observations in the SMASCS0723 field makes photometric redshift estimates uncertain (e.g. Arrabal Haro et al. 2023). We therefore consider these as lower confidence objects requiring follow-up confirmation to be considered part of this protocluster. The positions of our sample can be seen in the RGB image shown in Figure 1, falling within a $\sim 100 \times 200$ pkpc^2 region.

Finally, we note that the photometry of PW3 satisfies the photometric diagnostics of so-called "little red dots" (Matthee et al. 2024), which is discussed in detail in Appendix B. The strong Balmer breaks and red rest-optical slopes of LRDs are likely driven by dense gas around a central black hole (Inayoshi & Maiolino 2025; Ji et al. 2025; D'Eugenio et al. 2025; Naidu et al. 2025). As such, it is inappropriate to perform SED-fitting with stellar models, and hence, in the following section, we do not perform the same analysis of its properties as we do for the other galaxies in our sample.

3.1. Confirmation of an overdensity

Most protoclusters are identified thanks to their excessive quantities of UV-bright galaxies within small volumes of the early Universe. These are often characterised by the number of observed galaxies relative to the expected number from the integral of the UV luminosity function ($\delta + 1 = N_{\rm obs}/N_{\rm exp}$). To measure the UV luminosity, and the UV-slope, of our sample, we fit the F150W, F200W and F277W filters with a power law ($f_\lambda \propto \lambda^\beta$), with Monte Carlo uncertainty propagation, and evaluate the model at $\lambda = 0.15\mu$m. The inferred UV-slopes and luminosities are reported in Table 1.

In order to estimate the UV overdensity, we utilise a volume that contains all of our sample: a radius of $R = 0.1$ pMpc and a redshift interval of $7.65 < z < 7.67$ (~ 0.7 pMpc), resulting in a volume of ~ 19 cMpc^3. When we integrate the UVLF to the 5σ limiting magnitude ($m_{\rm F150W} \sim 29.7$ AB), within this volume, we find $\delta \sim 200$.

We additionally show the UVLF of SMACS-PC-z7p7 in Figure 3 and compare it to the nominal UVLF (Harikane et al. 2024), finding it to be $\sim$ 300 times in excess of the nominal UVLF. We additionally compare to the UVLF of A2744-PC-z7p9, measured over the same central volume of ~ 19 cMpc^3. The normalisation of the local UVLF of A2744-PC-z7p9 is around a factor of six greater than SMACS-PC-z7p7 in the regime where the photometric selection has a high completeness, indicating that SMACS-PC-z7p7 is a slightly less extreme environment than A2744-PC-z7p9.

We additionally compare to simulations of overdense environments from Kulkarni & Choudhury (2011) and Trebitsch et al. (2021)[6]. Both of the simulations show a shallower evolution of the UVLF relative to the nominal UVLF. The simulations show an excess in the brightest objects, which are known to be biased to overdense environments (Jespersen et al. 2025), and a deficit of fainter objects, expected due to the excessive Lyman-Werner production in these environments, suppressing star formation in low-mass DM haloes. The SMACS0723 UVLF is consistent with the shape of both the nominal UVLF (scaled by a factor of 300) and the shallower UVLF from simulations of overdense environments; however, we do note a slight excess in UV-bright galaxies, in line with the latter.

Given the small volumes being considered, it is important to quantify the effects of cosmic variance. We use *QuickCV* (New-

[4] https://github.com/ivkram/specvizitor
[5] https://dawn-cph.github.io/dja/imaging/v7/

[6] The UVLF of Obelisk at $z = 7.9$, shown in Figure 3, is taken from Witten et al. (2025b), which focuses on the central $R = 2$ cMpc of the protocluster and applies a dust prescription with a Small Magellanic Cloud-like extinction law, described in Trebitsch et al. in prep. and Volonteri et al. (2025).

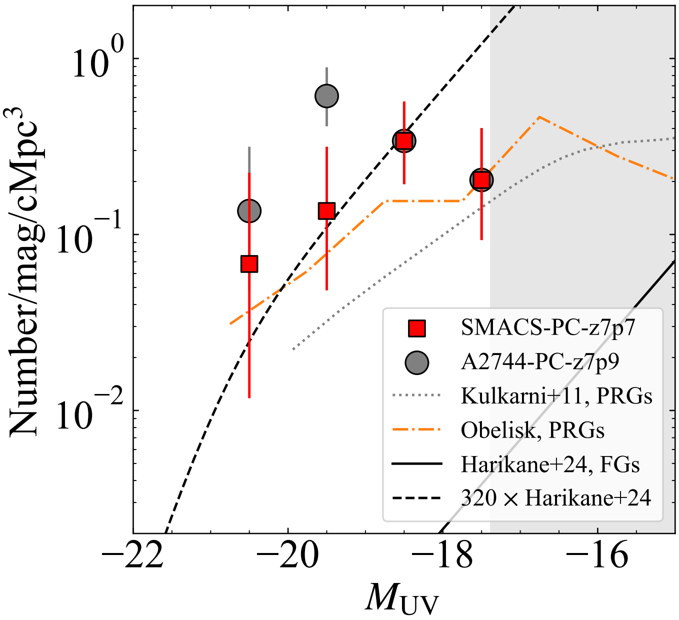

Fig. 3. The UV luminosity function of galaxies within SMACS-PC-z7p7 (red squares), compared to the UVLF of another $z \sim 8$ protocluster, A2744-PC-z7p9 (Witten et al. 2025b, grey circular points), calculated within the same central volume. The UVLF of other overdense environments from simulations are shown (Trebitsch et al. 2021; Kulkarni & Choudhury 2011, orange dash-dotted and grey dotted lines, respectively), that have a similar shallow gradient to that seen in SMACS-PC-z7p7. The grey shaded region represents the 5σ depth in the UV-continuum. Relative to the nominal UVLF of $z \sim 8$ galaxies from Harikane et al. (2024) (black solid line), the UVLF of SMACS-PC-z7p7 appears to be ~ 300 times higher (black dashed line).

man & Davis 2002) to estimate the DM variance of our volume (24%), and assuming a galaxy bias of $b_g = 8$ from Shuntov et al. (2025), we find that at 1σ cosmic variance can account for a tripling in the expected number of galaxies within this small volume. As such, our observed overdensity, $\delta = 200$, is a $\sim 60\sigma$ outlier from the cosmic variance. If we instead consider a significantly larger volume than that occupied by the SMACS-PC-z7p7 galaxies, corresponding to the Lagrangian radius from Chiang et al. (2017) ($R_L = 10$ cMpc), the overdensity falls to $\delta = 3$, which is a 2.6σ outlier from cosmic variance. We note that the overdensity parameter of A2744-PC-z7p9, when calculated over the same large volume, falls to a similarly low value of $\delta \sim 8$. This large volume is far in excess of the expected sizes of the cores of protoclusters at these redshifts (Chiang et al. 2017). Therefore, regardless of the volume selected, these regions appear to be significantly overdense relative to the nominal UVLF.

While establishing the UV luminosity of our sample, we also obtain the UV-slope of each galaxy (except for PW6 which resides in the newly imaged region of SMACS0723 and thus only has F090W, F115W and F444W imaging available). This reveals a diversity in the UV-slopes of our sample, ranging from $-2.2 < \beta < -1.4$. The majority of SMACS-PC-z7p7 galaxies have UV-slopes that are largely consistent with the average UV-slope measured from photometry at this redshift ($\beta \sim -2.2$ at $z \sim 7.6$; Austin et al. 2024). These are consistent with the UV-slopes measured for non-core resident galaxies in A2744-PC-z7p9. However, two galaxies in our sample show distinctly redder UV-slopes, $\beta = -1.4$, PW3 and PW4. As discussed earlier, PW3 is likely an LRD, and hence we do not interpret its UV-slope. PW4 is the most UV-luminous galaxy in our sample, and while a mild increase in the UV-slope is expected with M_{UV} (e.g. Saxena et al. 2024), this object is redder than expected given its UV luminosity. Given its luminosity and red UV-slope we hypothesis that PW4 likely represents the central galaxy resident within the core of this protocluster, akin to the massive core galaxies with red UV-slopes reported for A2744-PC-z7p9 in Witten et al. (2025b).

4. Galaxy properties

We utilise the SED-fitting code PROSPECTOR (Johnson et al. 2021) to simultaneously fit the photometric data and the Hβ and [O III] emission line fluxes. We use the same 16-parameter model as Witten et al. (2025a) (based on Tacchella et al. 2023b), which most notably includes a non-parametric star-formation history with a continuity prior (Leja et al. 2019) and a flexible two-component dust attenuation model (Conroy 2013).

Following Witten et al. (2025b), we avoid fitting the NIRCam filter covering the Lyman-α break. This is due to the potential for excessive damping around the Lyman-α break caused by significant neutral hydrogen column densities (e.g. Heintz et al. 2024b). This damping is not modelled by PROSPECTOR and is especially prominent in massive dark matter haloes, and hence, overdense environments (Heintz et al. 2024a; Witten et al. 2025a; Li et al. 2025a; Gelli et al. 2025). Therefore, we do not include the F115W filter in our PROSPECTOR SED-fitting.

The stellar masses inferred from this SED-fitting are reported in Table 1 and the best-fit SED and SFH can be found in Figure A.1. Note that the results of SED-fitting the galaxy PW3 are omitted and are discussed further in Section B.1.

4.1. Neutral hydrogen column densities

As discussed above, we intentionally omit the F115W filter from our SED-fitting given that we anticipate potential damping from high neutral hydrogen column densities that PROSPECTOR does not model. Given this, we can utilise our best-fit PROSPECTOR model to estimate the required damping, and hence neutral hydrogen column density, to match the observed F115W flux. We first apply an IGM attenuation curve to the model, assuming a neutral fraction of one and no ionised bubble following Mason & Gronke (2020),which maximises the impact of the IGM and hence minimises the impact of the DLA (thus our N_{HI} estimate is technically a lower bound). We then assume a Voigt-Hjerting profile for the DLA absorption, which is valid for high N_{HI}, utilising Equation 9 of Smith et al. (2015). Finally, we iterate over a grid of N_{HI} to find the required damping to the model spectrum to match the observed F115W flux.

The results of this can be seen in Figure 4 and are reported in Table 1. While PW1 has an inferred $N_{HI} > 10^{21.5}$ cm^{-2}, this amounts to only $\sim 10\%$ of the sample, compared to $\sim 60\%$ of galaxies in A2744-PC-z7p9. Notably, the galaxy impacted by the highest neutral hydrogen column density is located within the most clustered region of SMACS-PC-z7p7, including PW1, PW2, PW7 and PW8, a result that is also seen in A2744-PC-z7p9 (Witten et al. 2025b). Excess emission relative to the model spectrum, beyond observational uncertainties in the F115W filter, are seen in three of SMACS-PC-z7p7-resident galaxies. This excess can be due to either uncertainties in our PROSPECTOR models or due to Lyα emission contaminating the F115W filter.

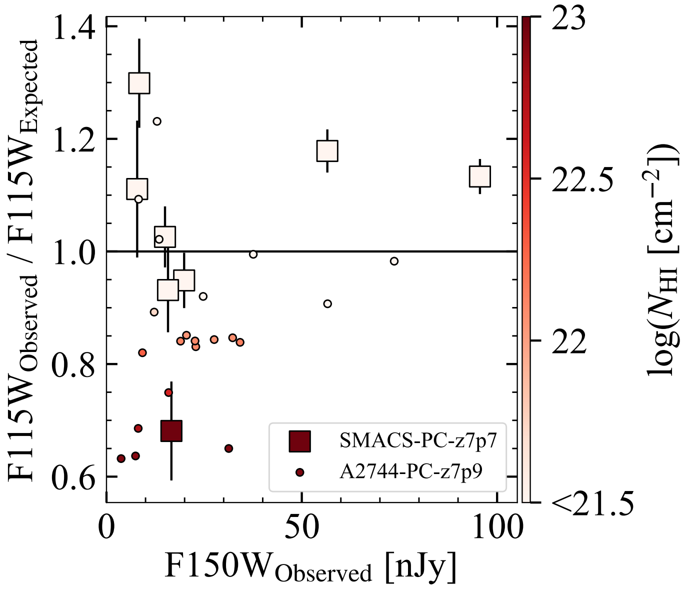

Fig. 4. The ratio of the observed to expected flux in the F115W filter, where increasing neutral hydrogen column density (colorbar) produces excessive damping of the Lyman-α break, suppressing the observed flux in the F115W filter. The photometry of SMACS-PC-z7p7-resident galaxies are shown by squares, while A2744-PC-z7p9-resident galaxies are identified with circles (Witten et al. 2025b). While two galaxies in SMACS-PC-z7p7 show extreme column densities, this is a much smaller fraction of the sample than those with extreme column densities in A2744-PC-z7p9.

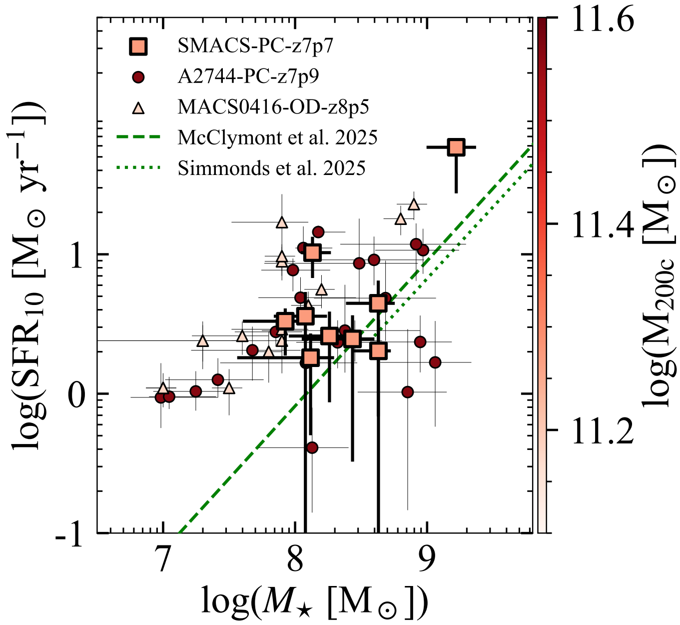

Fig. 5. The star-forming main sequence (SFMS) of galaxies in SMACS-PC-z7p7 (squares), A2744-PC-z7p9 (circles; Witten et al. 2025b) and MACS0416-OD-z8p5 (triangles; Fudamoto et al. 2025a), compared to the SFMS of field galaxies measured from observations (Simmonds et al. 2025, green dotted line) and simulations (McClymont et al. 2025, green dashed line). The SFMS is colored based on its virial mass, estimated using the method discussed in Section 5. While the most massive galaxies in A2744-PC-z7p9 are below the SFMS, all galaxies in SMACS-PC-z7p7 and MACS0416-OD-z8p5 fall on or above the SFMS of field galaxies.

4.2. Star-formation histories

Thanks to our combined fitting of both photometry and our constraints on [O III] and Hβ emission, we can break the degeneracy in the Balmer break or strong emission lines scenario (e.g. Roberts-Borsani et al. 2020). With the measurement of the rest-optical continuum, we can place improved constraints on the SFHs of resident galaxies. It is clear that while some of our galaxies (PW2, PW7 and PW13) show some evidence of a mild Balmer break, their SFHs are still consistent with a recent and ongoing burst of star formation (see Figure A.1), as has previously been suggested for PW4 and PW5 from Tacchella et al. (2023b). These objects exclusively show $\mathrm{SFR}_{10}/\mathrm{SFR}_{100} > 1$, i.e. rising SFHs, which is at odds with the wide range of SFHs present in the A2744-PC-z7p9 (Witten et al. 2025b).

Utilising these inferred SFHs, we place SMACS-PC-z7p7-resident galaxies on the star-forming main sequence (SFMS) in Figure 5. We compare these to protocluster-resident galaxies from A2744-PC-z7p9 (Witten et al. 2025b) and MACS0416-OD-z8p5 (Fudamoto et al. 2025a), and field galaxies from observations (Simmonds et al. 2025) and simulations (McClymont et al. 2025). Notably, the entire sample of galaxies in SMACS-PC-z7p7 are consistent with, or above, the SFMS of field galaxies. While observations are biased to detecting highly star-forming low-mass galaxies, at the high-mass end ($M_\star \gtrsim 10^9$ M$_\odot$), observations are highly complete with deep NIRCam imaging (Simmonds et al. 2025), which is the case for both SMACS0723 and Abell 2744 (both with similar F115W imaging depths; Bezanson et al. 2024). Therefore, the lack of galaxies below the SFMS at high masses is noteworthy. This is at odds with the case for galaxies within A2744-PC-z7p9, which have a large scatter around the SFMS, and at the highest masses fall below the SFMS. This suggests that instead of suppressing star formation, like in some galaxies resident in A2744-PC-z7p9, residency within SMACS-PC-z7p7 actually enhances star-formation rates. This is likely as a result of the significant gas accretion that is known to occur in these environments, as supported by the detection of extreme hydrogen column densities in PW1, without the onset of significant environmental effects that can act to suppress star formation.

5. Halo masses

We note that the method for estimating DM halo masses for protocluster environments at high redshift are notoriously inhomogeneous. Protoclusters are often characterised by dense cores of massive galaxies, meaning the assumption of a single central massive galaxy is inappropriate. We therefore utilise the TNG300 (Pillepich et al. 2018; Nelson et al. 2018; Naiman et al. 2018; Marinacci et al. 2018; Springel et al. 2018) and TNG-Cluster (Nelson et al. 2024) simulations to study the stellar mass within the virial radius as a diagnostic of halo mass. We calculate this by summing the stellar masses of subhaloes that fall within $R < R_{200c}$ (the virial radius) of the most massive galaxy in the halo. In Figure 6 we show the stellar mass within the virial radius as a function of the virial mass. We fit the haloes at $z \sim 7.6$, with stellar masses greater than $M_\star > 10^{8.2}$ M$_\odot$, with a linear fit ($\log_{10} M_{200c} = a \times \log_{10} M_\star + b$; $a = 0.49$, $b = 6.86$) and find a scatter around the best-fit of 0.13 dex. We see a mild discrepancy between the Behroozi et al. (2019) stellar-to-halo mass relation, which is calculated using only the stellar mass of the

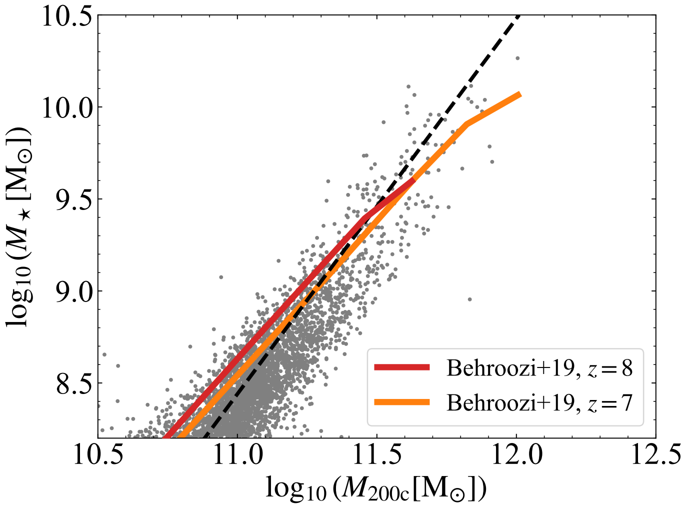

Fig. 6. The stellar mass within the virial radius as a function of the halo mass of haloes in the TNG300 and TNG-Cluster simulations. Haloes at $z = 7.6$ are indicated by grey points. We fit these data points with a linear fit, shown by a dashed black line. Finally, we also show the stellar-to-halo mass relation (SHMR) from Behroozi et al. (2019) at $z = 7$ (orange solid line) and $z = 8$ (red solid line). Our adapted SHMR provides a diagnostic for the virial mass based on the stellar mass within the virial radius.

central galaxy, in contrast to our relation, using the total stellar mass within the virial radius. This offset is also impacted by the underestimation of stellar mass driven by the lower resolution of simulations like TNG300 and TNG-Cluster (e.g. Pillepich et al. 2018; Vogelsberger et al. 2020). This can result in offsets of up to 0.3 dex at $z \sim 10$ (Kannan et al. 2023).

The virial radii of the most massive haloes in TNG300 and TNG-Cluster at $z \sim 8$ are $R_{200c} \lesssim 30$ pkpc; therefore, we utilise the total stellar mass within the same limiting virial radius from the most massive galaxy. In SMACS-PC-z7p7, PW4 represents the most massive galaxy ($\log_{10}(M_\star[M_\odot]) = 9.2^{+0.2}_{-0.2}$), and while an underlying galaxy population below the depth of current imaging is likely, it is unlikely to contribute significantly to the stellar mass within the virial radius. Using our best-fit linear model, we estimate the virial mass of SMACS-PC-z7p7 to be $\log_{10}(M_{200c}[M_\odot]) = 11.4^{+0.2}_{-0.2}$, with an uncertainty given by summing the stellar mass uncertainty and scatter in the stellar-to-halo mass relation in quadrature. We repeat this process for a number of well-known protocluster candidates at $z \gtrsim 7$, utilising reported stellar masses from Fudamoto et al. (2025a); Witten et al. (2025b); Li et al. (2025a); Arribas et al. (2024). Their inferred virial masses are shown in Figure 7.

5.1. Halo mass evolution

We track haloes with current-day masses of $M_{200c} > 10^{12.5}$ $M_\odot$ in TNG300 to chart the evolution of the virial mass as a function of redshift. In addition to our TNG300 analysis, we also utilise all current-day clusters in the TNG-Cluster simulation (reported in Nelson et al. 2024), in order to access those rarest, most massive DM haloes. We use the `SubLink` merger trees (Rodriguez-Gomez et al. 2015) to follow the most massive progenitor branch of the $z = 0$ haloes to find their progenitor haloes out to $z = 10$. Figure 7 shows this evolution, where we interpolate the evolution of individual haloes to a finer redshift grid to fill voids in the redshift range of the TNG-Cluster and TNG300 simulations. We additionally note that there do exist current-day clusters that grow their virial mass by orders of magnitude in fewer than 100 Myr, presumably by significant merger events. While the evolution of such systems is interesting, they do not represent the evolutionary pathway of these already massive haloes at high redshift, and therefore, they are removed from our analysis. Each hexagonal bin in Figure 7 is coloured based on the median present-day mass of haloes that fall within said bin.

Additionally, we take all $z = 7.6$ haloes with virial masses in three halo mass bins – $\log_{10}(M_{200c,\, z=7.6}\ [M_\odot]) > 11.5$, $11.5 > \log_{10}(M_{200c,\, z=7.6}\ [M_\odot]) > 11.25$ and $11.25 > \log_{10}(M_{200c,\, z=7.6}\ [M_\odot]) > 11$ – and track their descendants forward in time. Haloes within these $z = 7.6$ virial mass bins evolve to become current-day haloes of masses $\log_{10}(M_{200c,\, z=0}\ [M_\odot]) = 14.6\pm0.6$, 13.7 ± 0.7 and 13.3 ± 0.7, respectively. Using the uncertainty on the virial mass of SMACS-PC-z7p7 at $z = 7.66$, we find the median current-day mass of haloes within that mass range to be $\log_{10}(M_{200c,\, z=0}[M_\odot]) = 13.7 \pm 0.6$. Assuming SMACS-PC-z7p7 follows this median evolutionary pathway, this places it in line to become a low-mass cluster at $z = 0$, consistent with a Fornax-type cluster ($M_{200c,\, z=0} = 0.7 - 3 \times 10^{14}$ $M_\odot$), within uncertainties. Instead, the observed virial mass of A2744-PC-z7p9 places it on course to become $\log_{10}(M_{200c,\, z=0}[M_\odot]) = 14.3 \pm 0.7$ at current-day (assuming it follows the median evolutionary pathway), in line with the high-mass end of Fornax-type clusters or low mass Virgo-type clusters ($M_{200c,\, z=0} = 0.3 - 1 \times 10^{15}$ $M_\odot$).

Notably, while high mass haloes at $z > 7$ do appear to be a strong diagnostic of high virial masses at $z = 0$, the reverse is not as clear. We find examples of relatively low mass haloes at $z < 7$ that grow rapidly to become clusters at current-day. As such, the average growth histories of $z = 0$ clusters are steeper than the evolutionary pathways of high-mass haloes at $z > 7$.

6. Evidence for enhanced environmental effects with increasing halo mass

There are five $z \gtrsim 7$ protoclusters for which we can retrieve stellar mass and positional information to make our virial mass estimates. Two of these protoclusters have been claimed to host "evolved" (strong Balmer breaks and low equivalent width emission lines) galaxies (A2744-PC-z7p9, Witten et al. 2025b; SPT0311-58, Arribas et al. 2024) while the other three (SMACS-PC-z7p7, this work; JADES-GS-OD-7.2, Li et al. 2025a, Helton et al. 2024b; MACS0416-OD-z8p5, Fudamoto et al. 2025a) show evidence of highly star-forming galaxies dominated by young stellar populations. The latter are consistent with the typical properties of observed field galaxies at the same redshift (Roberts-Borsani et al. 2024).

Interestingly, the protoclusters that show evidence of evolved stellar populations are those with the highest virial masses, as determined by our adapted SHMR: A2744-PC-z7p9 is 0.2 dex more massive than SMACS-PC-z7p7, while SPT0311-58 is an order of magnitude more massive than SMACS-PC-z7p7. The SFMS shown in Figure 5 provides early evidence of suppression of star formation in the most massive protoclusters. While the most massive galaxies ($M_\star \sim 10^9$ $M_\odot$) in A2744-PC-z7p9 often fall on, or below, the SFMS, in the lower halo mass protoclusters (SMACS-PC-z7p7 and MACS0416-OD-z8p5) they fall above. In this mass regime, we expect to be highly complete and able to observe galaxies even in low SFR phases (Simmonds et al. 2025), and therefore, the differing scatter from the SFMS appears to indicate a suppression of star formation with increasing

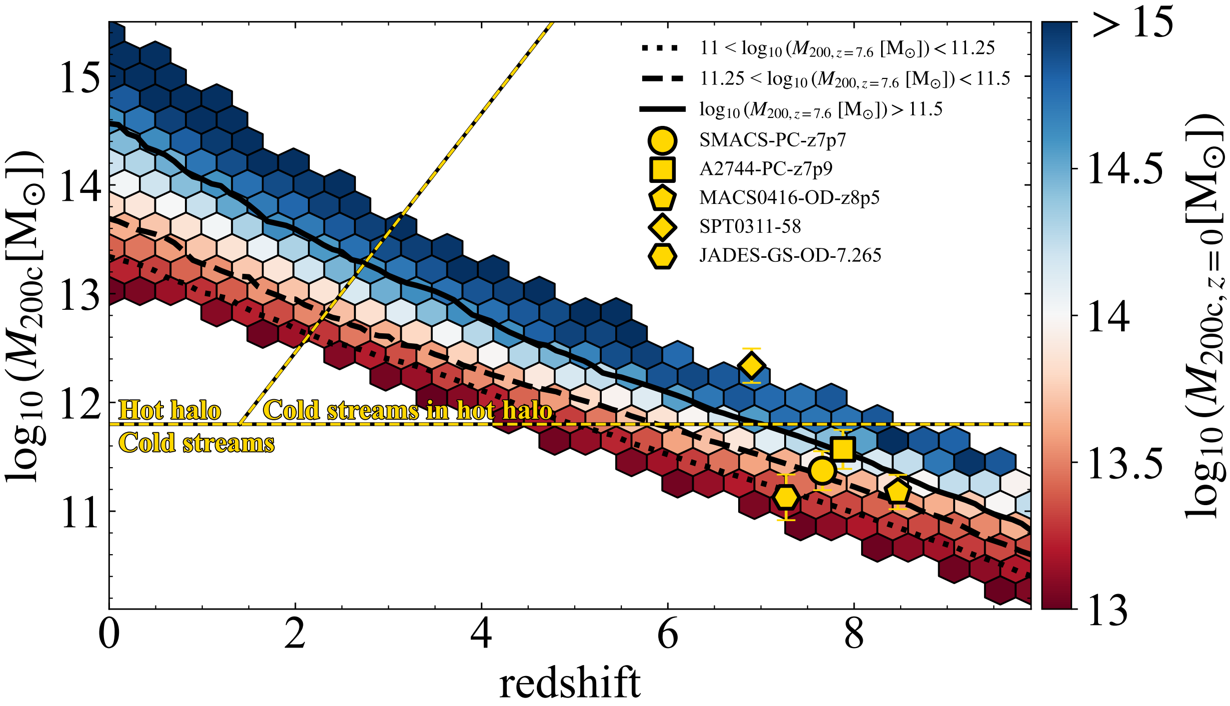

Fig. 7. The evolution of the virial mass of haloes in the TNG-Cluster and TNG300 simulations. The evolution of individual haloes have been interpolated to fill voids in the simulations' redshift grid. The colour of the hexagonal bins indicates the median current-day virial mass of the haloes within each bin, where these are $\log_{10}(M_{200c,\,z=0}\,[M_\odot]) > 13$. Additionally, overplot are the median evolutionary pathways of haloes binned by virial mass at $z = 7.6$: $\log_{10}(M_{200c,\,z=7.6}\,[M_\odot]) > 11.5$ (black solid line), $11.5 > \log_{10}(M_{200c,\,z=7.6}\,[M_\odot]) > 11.25$ (black dashed line) and $11.25 > \log_{10}(M_{200c,\,z=7.6}\,[M_\odot]) > 11.0$ (black dotted line). The different phases of CGM gas are indicated by the gold dashed lines from Dekel & Birnboim (2006). The gold data points indicate our estimate of the virial masses for $z \gtrsim 7$ protoclusters that have published stellar masses of resident galaxies (circle: SMACS-PC-z7p7, this work; square: A2744-PC-z7p9, Witten et al. 2025b; pentagon: MACS0416-OD-z8p5, Fudamoto et al. 2025a; diamond: SPT0311-58, Arribas et al. 2024; hexagon: JADES-GS-OD-7.265, Helton et al. 2024b,Li et al. 2025a).

halo mass. Although, we note this suppression is unlikely to lead to permanent quenching at this epoch.

In Figure 8, we show the offset from the SFMS_{10} (using the parametrisation of McClymont et al. 2025) of the galaxies identified in the aforementioned protoclusters (that have SFR_{10} and $M_\star$ measurements in the literature), as a function of protocluster halo mass. While these halo masses have large uncertainties, it is clear that with increasing halo mass there is an emergence of a population of galaxies that fall below the SFMS. An evolution in the average offset of each protocluster from the SFMS is also seen, lying above the SFMS at lower protocluster halo mass, to consistent with the SFMS at high halo masses.

We hypothesise that the enhanced SFR in the lower virial mass protoclusters are driven by the significant gas accretion that occurs in protocluster environments (Heintz et al. 2024a; Fudamoto et al. 2025b). However, with increasing virial mass comes increasing virial temperatures. At $M_{200c} \sim 10^{11.8}$ $M_\odot$, the virial temperature exceeds the temperatures at which cooling is effective (Mo et al. 2010), resulting in a heating of the CGM to temperatures of $T > 10^6$ K. While cold filamentary structures are dense enough at these redshifts ($z \gtrsim 3$) to penetrate into the hot halo and feed star formation, the net effect of the hot halo in suppressing star formation is poorly understood. Moreover, the formation of massive galaxies as these protoclusters evolve will result in enhanced stellar and AGN feedback, and prevalent galaxy-galaxy interactions (Marcelin et al. 2025) can significantly disrupt gas accretion. The combination of these feedback mechanisms can help to suppress star formation with increasing virial mass, and appear to become especially effec-

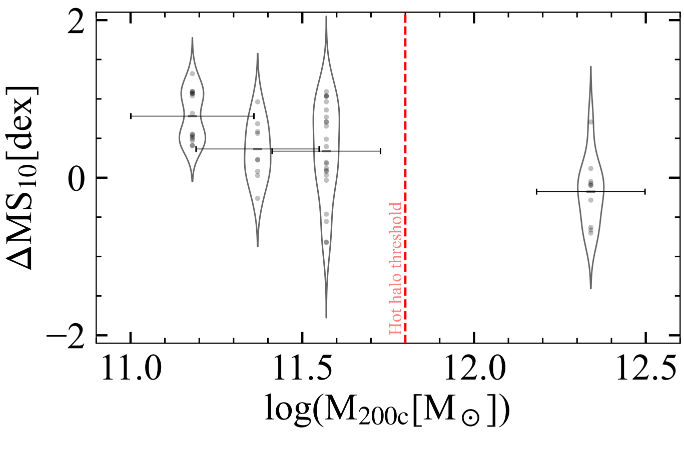

Fig. 8. The offset from the main sequence, $\Delta\mathrm{MS}_{10} = \log(\mathrm{SFR}_{10}/\mathrm{SFR}_{\mathrm{MS},10})$, at their respective redshifts, of different $z \gtrsim 7$ protoclusters, as a function of their virial masses. The protoclusters, in order of virial mass, shown in this plot (with references for stellar masses and SFR_{10}) are MACS0416-OD-z8p5 (Fudamoto et al. 2025a), SMACS-PC-z7p7 (this work), A2744-PC-z7p9 (Witten et al. 2025b) and SPT0311-58 (Arribas et al. 2024). The central bar indicates the average offset and the width of the bar shows the uncertainty in the halo mass. Individual galaxies are indicated by grey data points. The threshold at which a hot halo typically forms is indicated by a red dashed line (e.g. Dekel & Birnboim 2006). A population of galaxies that fall below the SFMS emerge with increasing halo mass, resulting in a decline in the average offset.

tive at $\log_{10}(M_{200c}[M_\odot]) \gtrsim 11.5$ (see Figure 8). This can result in the increased fraction of galaxies below the SFMS in the most massive haloes. In contrast, galaxies that reside further from the central core of these protoclusters can still have elevated SFR thanks to enhanced gas accretion and are less affected by these environmental effects that are more prominent in the cores of protoclusters.

7. Conclusions

We utilise recent *JWST* NIRCam F444W grism observations of the SMACS J0723.3-7327 field to confirm the photometric candidate protocluster environment from Laporte et al. (2022). These observations reveal six [O III]-emitting galaxies at $z = 7.66$, a further three high-confidence photometric candidates (in close proximity to these spectroscopically confirmed galaxies) and finally two $z \sim 7.6$ photometric candidates. These galaxies are resident within a 100×200 pkpc^2 area, with a redshift range of $\Delta z = 0.005$, resulting in an overdensity parameter of $\delta \sim 200$. The UVLF of this small volume is several hundred times (320×) the nominal UVLF, and is a factor of six times lower than that of the A2744-PC-z7p9 protocluster at $z = 7.88$ (Hashimoto et al. 2023; Morishita et al. 2023; Witten et al. 2025b).

We assess the properties of these galaxies using the SED-fitting code PROSPECTOR. SMACS-PC-z7p7-resident galaxies are exclusively characterised by a recent, ongoing burst of star formation ($SFR_{10}/SFR_{100} > 1$), with typically blue UV-slopes, given their redshift. This is at odds with the properties of galaxies resident in the $z = 7.88$ protocluster, A2744-PC-z7p9. Galaxies in A2744-PC-z7p9 have been reported to have SFHs that range from recent, ongoing bursts in the outskirts to continuous and even declining SFHs within the core of the protocluster (Witten et al. 2025b).

We find evidence of excessive damping around the Lyα-break, caused by extreme neutral hydrogen column densities ($N_{HI} > 10^{21.5}$ cm^{-2}), in one SMACS-PC-z7p7-resident galaxy. However, this is not widespread across our SMACS-PC-z7p7-resident sample, contrasting the high column densities seen in ∼ 60% of A2744-PC-z7p9-resident galaxies (Witten et al. 2025b).

In order to estimate the halo masses of SMACS-PC-z7p7 and other high-redshift protoclusters, we derive a relation between the stellar mass within the virial radius and the virial mass itself. In order to do so, we utilise the TNG-Cluster and TNG300 simulations, which facilitate an extension to higher virial masses at high redshift than typical SHMRs (e.g. Behroozi et al. 2019). With our adapted stellar(within the virial radius)-to-halo mass relation, the virial mass of SMACS-PC-z7p7 is estimated to be $\log_{10}(M_{200c}[M_\odot]) = 11.4 \pm 0.2$, 0.2 dex lower than that of A2744-PC-z7p9. Assuming that SMACS-PC-z7p7 follows the average evolutionary pathway of similar mass high-redshift haloes in these simulations, it is expected to become a low-mass Fornax-type cluster at $z = 0$, while A2744-PC-z7p9 appears to be a progenitor of a high-mass Fornax-type, or low-mass Virgo-type cluster. We additionally note that while high-mass ($\log_{10}(M_{200c}[M_\odot]) \gtrsim 11.5$), high-redshift ($z > 7$) haloes are on course to become clusters at present-day, clusters at present-day do not necessarily have high masses at high redshift. Instead, they can grow at rapid rates after beginning significant accretion at later cosmic epochs.

The average offset from the SFMS of galaxies resident within protoclusters appears to evolve with increasing halo mass. At low halo masses, protocluster-resident galaxies are largely found to lie above the SFMS, presumably as a result of the enhanced gas accretion which is expected in these environments. At large stellar masses ($M_\star > 10^9$ M$_\odot$), where we expect to be highly complete, with increasing protocluster halo mass, massive galaxies transition from sitting above the SFMS to having suppressed SFR relative to the SFMS.

We hypothesise that this emerging suppression of star formation is driven by multiple feedback processes that are related to increasing protocluster halo mass ($\log_{10}(M_{200c}[M_\odot]) \gtrsim 11.5$). These high halo masses can cause virial heating of the CGM gas, but also result in enhanced gas accretion and hence stellar and AGN feedback, and high merger rates (that can significantly impact the gas distribution around these core-resident galaxies, e.g. Witten et al. 2024). The exact combination of these processes that result in galaxies that appear more evolved is however uncertain.

In order to place stronger constraints on the evolution of protocluster-resident galaxies across differing halo masses, it is crucial to increase the number of robust high-redshift protocluster candidates. With existing simulations, like TNG-Cluster, it is easy to envisage a homogeneous selection criteria for high-redshift protoclusters. Applying these selection criteria to existing and future deep NIRCam imaging and grism campaigns will reveal a larger population of protocluster environments, the targeted follow-up of which will reveal the properties of resident galaxies. Combining this with the rapid advancement in large-scale cosmological radiative simulations in recent years, it will soon be possible to have a complimentary picture of galaxy evolution in extreme environments from both observational and theoretical vantage points.

Acknowledgements. The authors would like to thank Annalisa Pillepich and William McClymont for fruitful discussion and useful comments which improved this manuscript. The work presented in this paper is based on observations made with the NASA/ESA/CSA *James Webb* Space Telescope. The data were obtained from the Mikulski Archive for Space Telescopes at the Space Telescope Science Institute, which is operated by the Association of Universities for Research in Astronomy, Inc., under NASA contract NAS 5-03127 for *JWST*. These observations are associated with program 2736 and 4043. This work has received funding from the Swiss State Secretariat for Education, Research and Innovation (SERI) under contract number MB22.00072, as well as from the Swiss National Science Foundation (SNSF) through project grant 200020_207349. The Cosmic Dawn Center (DAWN) is funded by the Danish National Research Foundation under grant DNRF140. JSB acknowledges support from the Simons Collaboration on "Learning the Universe". WMB gratefully acknowledges support from DARK via the DARK fellowship. This work was supported by a research grant (VIL54489) from VILLUM FONDEN. LRI acknowledges support by the Science and Technology Facilities Council (STFC), ERC Advanced Grant 695671 "QUENCH" and the UKRI Frontier Research grant RISEandFALL.

References

Adams, N. J., Conselice, C. J., Ferreira, L., et al. 2023, Monthly Notices of the Royal Astronomical Society, Volume 518, Issue 3, pp.4755-4766, 518, 4755
Akins, H., Casey, C., Lambrides, E., et al. 2024, 243, 149.07, conference Name: American Astronomical Society Meeting Abstracts ADS Bibcode: 2024AAS...24314907A
Arrabal Haro, P., Dickinson, M., Finkelstein, S. L., et al. 2023, Nature, 622, 707
Arribas, S., Perna, M., Rodríguez Del Pino, B., et al. 2024, Astronomy & Astrophysics, 688, A146
Atek, H., Shuntov, M., Furtak, L. J., et al. 2023, Monthly Notices of the Royal Astronomical Society, 519, 1201
Austin, D., Conselice, C. J., Adams, N. J., et al. 2024, arXiv e-prints, arXiv:2404.10751
Baker, W. M., Ito, K., Valentino, F., et al. 2025, eprint arXiv:2509.09761, arXiv:2509.09761
Baxter, D. C., Coil, A. L., Nadler, E. O., et al. 2025, arXiv e-prints, arXiv:2504.03836
Behroozi, P., Wechsler, R. H., Hearin, A. P., & Conroy, C. 2019, MNRAS, 488, 3143
Behroozi, P. S., Wechsler, R. H., & Conroy, C. 2013, ApJ, 770, 57
Bennett, J. S. & Sijacki, D. 2020, MNRAS, 499, 597

Bezanson, R., Labbe, I., Whitaker, K. E., et al. 2024, The Astrophysical Journal, Volume 974, Issue 1, id.92, 14 pp., 974, 92
Blumenthal, G. R., Faber, S. M., Primack, J. R., & Rees, M. J. 1984, Nature, 311, 517
Bradley, L., Sipőcz, B., Robitaille, T., et al. 2025, astropy/photutils: 2.2.0
Brammer, G. 2019, Astrophysics Source Code Library, ascl:1905.001, aDS Bibcode: 2019ascl.soft05001B
Brammer, G. B., van Dokkum, P. G., & Coppi, P. 2008, The Astrophysical Journal, 686, 1503, publisher: IOP ADS Bibcode: 2008ApJ...686.1503B
Brinchmann, J. 2023, Monthly Notices of the Royal Astronomical Society, 525, 2087
Carnall, A. C., Begley, R., McLeod, D. J., et al. 2023, Monthly Notices of the Royal Astronomical Society, 518, L45
Castellano, M., Fontana, A., Treu, T., et al. 2023, The Astrophysical Journal, 948, L14, publisher: IOP ADS Bibcode: 2023ApJ...948L..14C
Champagne, J. B., Wang, F., Zhang, H., et al. 2025, The Astrophysical Journal, 981, 113, publisher: IOP ADS Bibcode: 2025ApJ...981..113C
Chiang, Y.-K., Overzier, R. A., Gebhardt, K., & Henriques, B. 2017, ApJ, 844, L23
Conroy, C. 2013, ARA&A, 51, 393
Curti, M., D'Eugenio, F., Carniani, S., et al. 2023, Monthly Notices of the Royal Astronomical Society, Volume 518, Issue 1, pp.425-438, 518, 425
Dekel, A. & Birnboim, Y. 2006, Monthly Notices of the Royal Astronomical Society, 368, 2
D'Eugenio, F., Maiolino, R., Perna, M., et al. 2025, BlackTHUNDER strikes twice: rest-frame Balmer-line absorption and high Eddington accretion rate in a Little Red Dot at $z=7.04$, publication Title: arXiv e-prints ADS Bibcode: 2025arXiv250311752D
Donnan, C. T., McLeod, D. J., Dunlop, J. S., et al. 2023, MNRAS, 518, 6011
Fudamoto, Y., Helton, J. M., Lin, X., et al. 2025a, eprint arXiv:2503.15597, arXiv:2503.15597
Fudamoto, Y., Nakazato, Y., Ceverino, D., et al. 2025b, Early massive galaxy formation in the core of a galaxy protocluster 650 million years after the Big Bang, arXiv:2510.11770 [astro-ph]
Furtak, L. J., Labbé, I., Zitrin, A., et al. 2024, Nature, 628, 57
Furtak, L. J., Secunda, A. R., Greene, J. E., et al. 2025, Investigating photometric and spectroscopic variability in the multiply-imaged Little Red Dot A2744-QSO1, publication Title: arXiv e-prints ADS Bibcode: 2025arXiv250207875F
Furtak, L. J., Zitrin, A., Plat, A., et al. 2023, The Astrophysical Journal, 952, 142
Gelli, V., Mason, C., Pallottini, A., et al. 2025, Neutral hydrogen in and around galaxies during the Epoch of Reionization, arXiv:2510.01315 [astro-ph]
Greene, J. E., Labbe, I., Goulding, A. D., et al. 2024, The Astrophysical Journal, 964, 39, publisher: IOP ADS Bibcode: 2024ApJ...964...39G
Harikane, Y., Nakajima, K., Ouchi, M., et al. 2024, ApJ, 960, 56
Harikane, Y., Ouchi, M., Oguri, M., et al. 2023, The Astrophysical Journal Supplement Series, 265, 5
Harikane, Y., Ouchi, M., Ono, Y., et al. 2019, ApJ, 883, 142
Hashimoto, T., Álvarez Márquez, J., Fudamoto, Y., et al. 2023, The Astrophysical Journal Letters, 955, L2
Heintz, K. E., Bennett, J. S., Oesch, P. A., et al. 2024a, arXiv e-prints
Heintz, K. E., Watson, D., Brammer, G., et al. 2024b, Science, 384, 890
Helton, J. M., Sun, F., Woodrum, C., et al. 2024a, The Astrophysical Journal, 962, 124
Helton, J. M., Sun, F., Woodrum, C., et al. 2024b, Identification of High-Redshift Galaxy Overdensities in GOODS-N and GOODS-S, arXiv:2311.04270
Hopkins, P. F., Murray, N., Quataert, E., & Thompson, T. A. 2010, Monthly Notices of the Royal Astronomical Society, 401, L19, publisher: OUP ADS Bibcode: 2010MNRAS.401L..19H
Inayoshi, K. & Maiolino, R. 2025, The Astrophysical Journal, 980, L27, publisher: IOP ADS Bibcode: 2025ApJ...980L..27I
Ivey, L. R., Scholtz, J., Danhaive, A. L., et al. 2025, eprint arXiv:2507.14936, arXiv:2507.14936
Jespersen, C. K., Steinhardt, C. L., Somerville, R. S., & Lovell, C. C. 2025, The Astrophysical Journal, 982, 23, arXiv:2403.00050 [astro-ph]
Ji, X., Maiolino, R., Übler, H., et al. 2025, BlackTHUNDER – A non-stellar Balmer break in a black hole-dominated little red dot at $z=7.04$, publication Title: arXiv e-prints ADS Bibcode: 2025arXiv250113082J
Johnson, B. D., Leja, J., Conroy, C., & Speagle, J. S. 2021, ApJS, 254, 22
Kannan, R., Springel, V., Hernquist, L., et al. 2023, Monthly Notices of the Royal Astronomical Society, 524, 2594
Kashino, D., Lilly, S. J., Matthee, J., et al. 2023, The Astrophysical Journal, 950, 66, arXiv:2211.08254 [astro-ph]
Katz, N., Keres, D., Davé, R., & Weinberg, D. H. 2003, in The IGM/Galaxy Connection, ed. J. L. Rosenberg & M. E. Putman, Vol. 281 (Dordrecht: Springer Netherlands), 185–192, series Title: Astrophysics and Space Science Library
Keres, D., Katz, N., Weinberg, D. H., & Dave, R. 2005, Monthly Notices of the Royal Astronomical Society, 363, 2
Kokorev, V., Caputi, K. I., Greene, J. E., et al. 2024, The Astrophysical Journal, 968, 38, publisher: IOP ADS Bibcode: 2024ApJ...968...38K
Kulkarni, G. & Choudhury, T. R. 2011, Monthly Notices of the Royal Astronomical Society, 412, 2781, publisher: OUP ADS Bibcode: 2011MNRAS.412.2781K
Labbe, I., Greene, J. E., Bezanson, R., et al. 2023, arXiv e-prints
Laporte, N., Ellis, R. S., Boone, F., et al. 2017, ApJ, 837, L21
Laporte, N., Zitrin, A., Dole, H., et al. 2022, Astronomy and Astrophysics, 667, L3, aDS Bibcode: 2022A&A...667L...3L
Leja, J., Carnall, A. C., Johnson, B. D., Conroy, C., & Speagle, J. S. 2019, ApJ, 876, 3
Li, Q., Conselice, C. J., Austin, D., et al. 2025a, eprint arXiv:2508.08037, arXiv:2508.08037
Li, Q., Conselice, C. J., Sarron, F., et al. 2025b, Monthly Notices of the Royal Astronomical Society, Volume 539, Issue 2, pp. 1796-1819, 24 pp., 539, 1796
Lim, S., Tacchella, S., Schaye, J., et al. 2024, Monthly Notices of the Royal Astronomical Society, Volume 532, Issue 4, pp.4551-4569, 532, 4551
Ma, Y., Greene, J. E., Setton, D. J., et al. 2024, UNCOVER: 404 Error – Models Not Found for the Triply Imaged Little Red Dot A2744-QSO1, arXiv:2410.06257 [astro-ph]
Mandelker, N., Padnos, D., Dekel, A., et al. 2016, Monthly Notices of the Royal Astronomical Society, 463, 3921
Marcelin, L. C., Champagne, J. B., Wang, F., et al. 2025, arXiv:2505.18262 [astro-ph]
Marinacci, F., Vogelsberger, M., Pakmor, R., et al. 2018, Monthly Notices of the Royal Astronomical Society, 480, 5113
Mason, C. A. & Gronke, M. 2020, MNRAS, 499, 1395
Matthee, J., Naidu, R. P., Brammer, G., et al. 2024, ApJ, 963, 129
McClymont, W., Tacchella, S., Smith, A., et al. 2025, Monthly Notices of the Royal Astronomical Society, 544, 513
Meyer, R. A., Oesch, P. A., Giovinazzo, E., et al. 2024, Monthly Notices of the Royal Astronomical Society, 535, 1067, publisher: OUP ADS Bibcode: 2024MNRAS.535.1067M
Mo, H., van den Bosch, F. C., & White, S. 2010, Galaxy Formation and Evolution (Cambridge University Press)
Morishita, T., Liu, Z., Stiavelli, M., et al. 2025, The Astrophysical Journal, Volume 982, Issue 2, id.153, 15 pp., 982, 153
Morishita, T., Roberts-Borsani, G., Treu, T., et al. 2023, ApJ, 947, L24
Morishita, T. & Stiavelli, M. 2023, The Astrophysical Journal, 946, L35
Morokuma-Matsui, K., Yajima, H., & Abe, M. 2025, Monthly Notices of the Royal Astronomical Society, Volume 539, Issue 2, pp. 1834-1849, 16 pp., 539, 1834
Naidu, R. P., Matthee, J., Katz, H., et al. 2025, A "Black Hole Star" Reveals the Remarkable Gas-Enshrouded Hearts of the Little Red Dots, publication Title: arXiv e-prints ADS Bibcode: 2025arXiv250316596N
Naidu, R. P., Matthee, J., Kramarenko, I., et al. 2024, All the Little Things in Abell 2744: $>$1000 Gravitationally Lensed Dwarf Galaxies at $z=0-9$ from JWST NIRCam Grism Spectroscopy, publication Title: arXiv e-prints ADS Bibcode: 2024arXiv241001874N
Naiman, J. P., Pillepich, A., Springel, V., et al. 2018, Monthly Notices of the Royal Astronomical Society, 477, 1206
Nelson, D., Pillepich, A., Ayromlou, M., et al. 2024, Introducing the TNG-Cluster Simulation: overview and physical properties of the gaseous intracluster medium, arXiv:2311.06338 [astro-ph]
Nelson, D., Pillepich, A., Springel, V., et al. 2018, Monthly Notices of the Royal Astronomical Society, 475, 624
Newman, J. A. & Davis, M. 2002, The Astrophysical Journal, 564, 567, publisher: IOP ADS Bibcode: 2002ApJ...564..567N
Oesch, P. A., Brammer, G., Naidu, R. P., et al. 2023, Monthly Notices of the Royal Astronomical Society, 525, 2864
Pascale, M., Frye, B. L., Diego, J., et al. 2022, arXiv e-prints, arXiv:2207.07102
Peebles, P. J. E. 1982, ApJ, 263, L1
Pillepich, A., Nelson, D., Hernquist, L., et al. 2018, Monthly Notices of the Royal Astronomical Society, 475, 648
Pontoppidan, K. M., Barrientes, J., Blome, C., et al. 2022, The Astrophysical Journal Letters, 936, L14, publisher: The American Astronomical Society
Pudoka, M., Wang, F., Fan, X., et al. 2024, The Astrophysical Journal, 968, 118, publisher: IOP ADS Bibcode: 2024ApJ...968..118P
Pudoka, M., Wang, F., Fan, X., et al. 2025, The Astrophysical Journal, 987, 198, publisher: IOP ADS Bibcode: 2025ApJ...987..198P
Roberts-Borsani, G., Treu, T., Shapley, A., et al. 2024, The Astrophysical Journal, Volume 976, Issue 2, id.193, 24 pp., 976, 193
Roberts-Borsani, G. W., Ellis, R. S., & Laporte, N. 2020, MNRAS, 497, 3440
Rodriguez-Gomez, V., Genel, S., Vogelsberger, M., et al. 2015, Monthly Notices of the Royal Astronomical Society, 449, 49, publisher: OUP ADS Bibcode: 2015MNRAS.449...49R
Saxena, A., Cameron, A. J., Katz, H., et al. 2024, eprint arXiv:2411.14532, arXiv:2411.14532

Scholtz, J., Witten, C., Laporte, N., et al. 2024, Astronomy & Astrophysics, 687, A283
Shuntov, M., Oesch, P. A., Toft, S., et al. 2025, Astronomy and Astrophysics, 699, A231, publisher: EDP ADS Bibcode: 2025A&A...699A.231S
Simmonds, C., Tacchella, S., McClymont, W., et al. 2025, eprint arXiv:2508.04410, arXiv:2508.04410
Smith, A., Safranek-Shrader, C., Bromm, V., & Milosavljević, M. 2015, MNRAS, 449, 4336
Springel, V., Pakmor, R., Pillepich, A., et al. 2018, Monthly Notices of the Royal Astronomical Society, 475, 676
Sun, W., Ho, L. C., Zhuang, M.-Y., et al. 2024, The Astrophysical Journal, 960, 104, publisher: IOP ADS Bibcode: 2024ApJ...960..104S
Tacchella, S., Eisenstein, D. J., Hainline, K., et al. 2023a, ApJ, 952, 74
Tacchella, S., Finkelstein, S. L., Bagley, M., et al. 2022, ApJ, 927, 170
Tacchella, S., Johnson, B. D., Robertson, B. E., et al. 2023b, MNRAS, 522, 6236
Thomas, D., Maraston, C., Bender, R., & De Oliveira, C. M. 2005, The Astrophysical Journal, 621, 673
Trebitsch, M., Dubois, Y., Volonteri, M., et al. 2021, Astronomy & Astrophysics, 653, A154
Trump, J. R., Arrabal Haro, P., Simons, R. C., et al. 2023, The Astrophysical Journal, 945, 35
Valentino, F., Brammer, G., Gould, K. M. L., et al. 2023, The Astrophysical Journal, 947, 20, publisher: IOP ADS Bibcode: 2023ApJ...947...20V
Vogelsberger, M., Nelson, D., Pillepich, A., et al. 2020, Monthly Notices of the Royal Astronomical Society, 492, 5167
Volonteri, M., Trebitsch, M., Greene, J. E., et al. 2025, Astronomy & Astrophysics, Volume 695, id.A33, 16 pp., 695, A33
Wang, B., Leja, J., De Graaff, A., et al. 2024a, The Astrophysical Journal Letters, 969, L13
Wang, F., Yang, J., Hennawi, J. F., et al. 2024b, The Astrophysical Journal, 962, L11, publisher: IOP ADS Bibcode: 2024ApJ...962L..11W
Weibel, A., de Graaff, A., Setton, D. J., et al. 2025, The Astrophysical Journal, Volume 983, Issue 1, id.11, 16 pp., 983, 11
Witstok, J., Smit, R., Saxena, A., et al. 2024, Astronomy & Astrophysics, 682, A40
Witten, C., Laporte, N., Martin-Alvarez, S., et al. 2024, Nature Astronomy, 8, 384
Witten, C., McClymont, W., Laporte, N., et al. 2025a, Monthly Notices of the Royal Astronomical Society, Volume 537, Issue 1, pp.112-126, 537, 112
Witten, C., Oesch, P. A., McClymont, W., et al. 2025b, eprint arXiv:2507.06284, arXiv:2507.06284
Yajima, H., Abe, M., Khochfar, S., et al. 2021, Monthly Notices of the Royal Astronomical Society, 509, 4037, arXiv:2011.11663 [astro-ph]

Table A.1. Emission line fluxes obtained from F444W grism observations, not corrected for magnification.

ID	Flux (10^{-18} erg s^{-1} cm^{-2})		
	Hβ	[O III]4959	[O III]5007
PW1	0.6 ± 0.2	0.7 ± 0.4	2.0 ± 0.4
PW3	< 0.5	< 0.5	1.5 ± 0.5
PW4	5.3 ± 0.3	14.6 ± 0.6	43.5 ± 0.6
PW5	1.2 ± 0.2	3.5 ± 0.4	10.4 ± 0.4
PW6	< 0.6	1.2 ± 0.6	3.5 ± 0.6
PW8	0.6 ± 0.3	2.0 ± 0.6	6.1 ± 0.6

Appendix A: SEDs

In this appendix, we expand on our discussion of our SED-fitting of SMACS-PC-z7p7 galaxies. We first report the photometry that we measure for each galaxy in Table A.2 utilising the `Photutils` package.

We fit this photometry, in combination with the emission line fluxes reported in Table A.1, with the SED-fitting code `Prospector`. We show the best-fit SEDs and SFHs from this SED-fitting in Figure A.1. All of the galaxies in SMACS-PC-z7p7 are characterised by ongoing bursts in their SFHs. While some galaxies show evidence of mild Balmer breaks, which correspond to the galaxies with older stellar populations, the majority are characterised by having strong emission lines. The SFHs of PW4 and PW5 are consistent with those reported in (Tacchella et al. 2023b).

Appendix B: LRD diagnostics

Appendix B.1: Little Red Dot

In light of the detection of the compact, red source, PW3, we compare its photometric properties to the little red dot (LRD) selection criteria. We first fit the UV ($\sim 1-3\mu$m) and optical ($\sim 3-5\mu$m; where the emission lines fluxes have been subtracted from the F444W flux) continua with separate power laws (i.e. $f \propto \lambda^{\beta}$), revealing two distinct continuum slopes: $\beta_{\rm UV} = -1.4 \pm 0.2$ and $\beta_{\rm opt} = 1.5 \pm 0.3$. These appear in line with the UV and optical slopes of $z \sim 5-6.5$ LRDs reported in Matthee et al. (2024). Moreover, PW3 satisfies the widely utilised LRD selection criteria for galaxies at such redshifts - the "red2" criteria from Labbe et al. (2023):

$$\begin{aligned} &\text{F150W} - \text{F200W} < 0.8 \\ &\text{F277W} - \text{F356W} > 0.7 \\ &\text{F277W} - \text{F444W} > 1.0\,, \end{aligned}$$

which is combined with a compactness criteria: $f_{\rm F444W}(0''.4)/f_{\rm F444W}(0''.2) < 1.7$. PW3 satisfies all of the colour selection, as indicated in Figure B.2. Its compactness of $f_{\rm F444W}(0''.4)/f_{\rm F444W}(0''.2) = 1.06 \pm 0.02$ easily satisfies the requirement.

We start with the assumption that the SED of PW3 has only stellar origins. We utilise the SED-fitting code `PROSPECTOR`, as described in Section 3. This fitting yields a SFH that is dominated by a recent burst, over the previous ~ 20 Myrs, with a peak star-formation rate of $\sim 1,000 \mathrm{M}_{\odot}$/yr. The best-fit stellar mass is $\log_{10}(M_{\star}[\mathrm{M}_{\odot}]) = 10 \pm 0.1$, with a V-band dust attenuation of $A_V = 2.0^{+0.4}_{-0.2}$.

Before discussing the failure of our `PROSPECTOR` model to reproduce the extremely red rest-optical continuum of PW3, we first consider the implied stellar mass surface density of PW3 according to our model. The radial profile of the emission from PW3 in all filters can be described by the point-source function of said filter, as such yielding an effective radius in the F115W filter of $0''.03$. At $z = 7.67$ and accounting for a magnification of $\mu = 1.40$, this corresponds to $R_{\rm e} = 107$ pc. This implies PW3 has a stellar mass surface density of $\log_{10}(\Sigma_{*,<R_{\rm e}}[\mathrm{M}_{\odot}/\mathrm{kpc}^2]) > 11.4 \pm 0.1$, as shown in Figure B.1. LRDs have higher stellar mass surface densities than the general galaxy population when they are SED-fit assuming only a stellar model. Relative to a sample of $z > 7$ LRDs, from Akins et al. (2024), PW3 is among the highest stellar mass surface density objects, in part due to the magnification facilitating a smaller constraint on the effective radius. Similarly, A2744-QSO1 (an LRD whose rest-optical continuum has recently been shown to be driven by AGN emission; Furtak et al. 2024; Ji et al. 2025; Furtak et al. 2025; D'Eugenio et al. 2025) has a significantly smaller effective radius constraint thanks to lensing magnification, and as noted by Ma et al. (2024), this results in a stellar mass surface density in PW3 that is in excess of the maximum density observed in the local Universe and low-redshift galaxies ($\log_{10}(\Sigma_{*,<R_{\rm e}}[\mathrm{M}_{\odot}/\mathrm{kpc}^2]) \sim 11$; Hopkins et al. 2010). Moreover, the lower bound of the stellar mass surface density of PW3 is already in excess of the highest density object observed at $z > 7$ so far, RUBIES-UDS-QG-z7, a resolved, massive quiescent galaxy at $z = 7.29$ (Weibel et al. 2025).

While the `PROSPECTOR` model can fit the rest-UV-continuum well, it begins to struggle after the Balmer break (see Figure B.3). As it struggles to recreate the steep slope between the F277W and F444W detections, it overpredicts the F356W emission and significantly underpredicts the F444W emission. This failure to fit the optical continuum of LRDs with only a stellar model has been noted by Wang et al. (2024a), who invoke a combination of AGN accretion disk and stellar emission to fit the rest-optical continuum.

We note here that when we combine our best-fit UV-slope model with the rescaled spectrum of the black hole star (BH*) from Naidu et al. (2025) and our emission line constraints (see Table A.1), we produce an SED that is consistent with that observed for PW3, as shown in Figure B.3. Given our relative ease at producing an SED that is consistent with PW3 by invoking the BH* spectrum, and the inability of `Prosector`, even while assuming extreme stellar masses and dust attenuation, to reproduce the SED, we take this as further evidence that PW3 is an LRD.

Table A.2. Photometric measurements of protocluster-resident galaxies in nJy utilising an aperture size covering the F444W emission from each galaxy, without contamination from nearby sources. 1-σ limiting depths are indicated in the case of non-detection. OOF indicates a galaxy is outside of the field of imaging. All values included are not corrected for magnification.

ID	F090	F115	F150	F200	F277	F356	F444
PW1	< 2.79	13.11 ± 1.69	24.43 ± 3.40	26.17 ± 2.64	26.89 ± 2.66	35.80 ± 2.80	55.69 ± 1.38
PW2	< 1.71	9.39 ± 1.03	11.55 ± 1.98	12.35 ± 1.62	12.72 ± 1.42	18.15 ± 1.53	31.14 ± 0.91
PW3	< 1.14	9.09 ± 0.73	10.34 ± 1.90	12.26 ± 1.55	17.27 ± 1.67	35.50 ± 1.83	100.53 ± 0.95
PW4	< 3.36	90.38 ± 2.48	131.94 ± 3.80	135.87 ± 3.25	185.09 ± 2.80	242.78 ± 2.94	617.51 ± 2.05
PW5	< 2.48	72.81 ± 2.37	78.59 ± 2.80	71.73 ± 2.33	73.21 ± 1.98	81.95 ± 1.97	167.56 ± 1.40
PW6	< 4.08	40.25 ± 2.64	OOF	OOF	OOF	OOF	74.79 ± 2.23
PW7	< 1.71	19.66 ± 1.04	22.02 ± 2.04	21.92 ± 1.69	21.47 ± 1.49	23.93 ± 1.60	32.75 ± 0.93
PW8	< 1.72	20.20 ± 1.05	29.22 ± 2.08	24.47 ± 1.71	26.98 ± 1.53	29.92 ± 1.63	57.69 ± 0.97
PW9	< 1.07	11.96 ± 0.73	11.74 ± 1.56	9.84 ± 1.31	12.51 ± 1.59	13.00 ± 1.64	24.90 ± 0.78
PW12	< 2.19	20.27 ± 1.63	25.52 ± 2.35	27.37 ± 1.97	27.61 ± 1.63	27.88 ± 1.64	35.32 ± 1.17
PW13	< 2.68	28.03 ± 1.52	27.21 ± 4.08	27.15 ± 3.35	23.11 ± 2.70	35.88 ± 2.87	36.20 ± 1.22

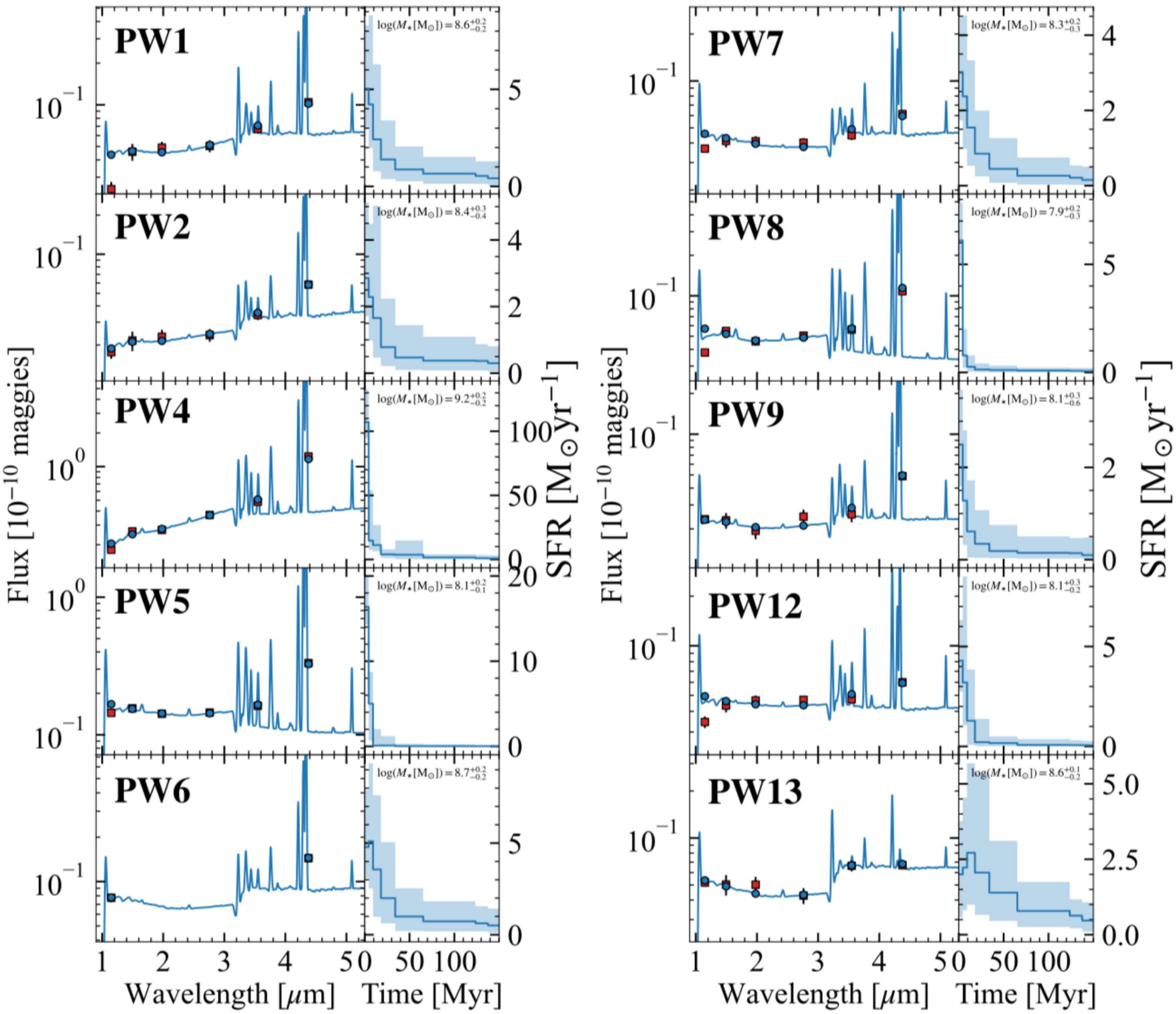

Fig. A.1. (Left:) The SEDs of SMACS-PC-z7p7-resident galaxies (red squares) and the best fit photometry (blue circles) and spectrum (blue solid line) from our `Prospector` modelling. (Right:) The corresponding best-fit SFH (blue solid line) and associated uncertainty (blue shaded region). The best-fit stellar mass is also indicated at the top of the panel.

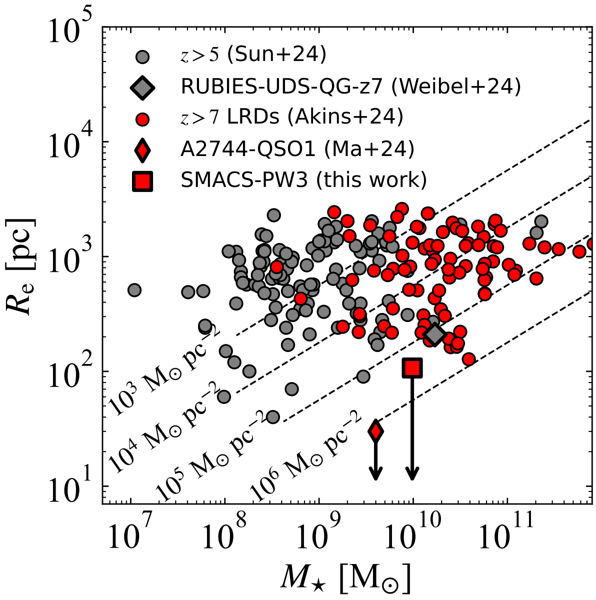

Fig. B.1. The stellar mass surface densities of galaxies at $z > 5$ in the CEERS survey (grey circle; Sun et al. 2024) and one of the most massive, compact, non-LRD objects (grey data points) at high-redshift (grey rotated square; Weibel et al. 2025). In red we indicate a sample of photometrically identified LRDs from (Akins et al. 2024) and two spectroscopically confirmed LRDs, A2744-QSO1 (red diamond; Ma et al. 2024) and SMACS-PW3 (red square; this work). It is clear that when modelled with purely stellar populations, the LRDs (red data points) have significantly higher stellar mass surface densities than the sample of $z > 5$ galaxies. Moreover, PW3 has a higher stellar mass surface density than even one of the most extreme density objects RUBIES-UDS-QG-z7.

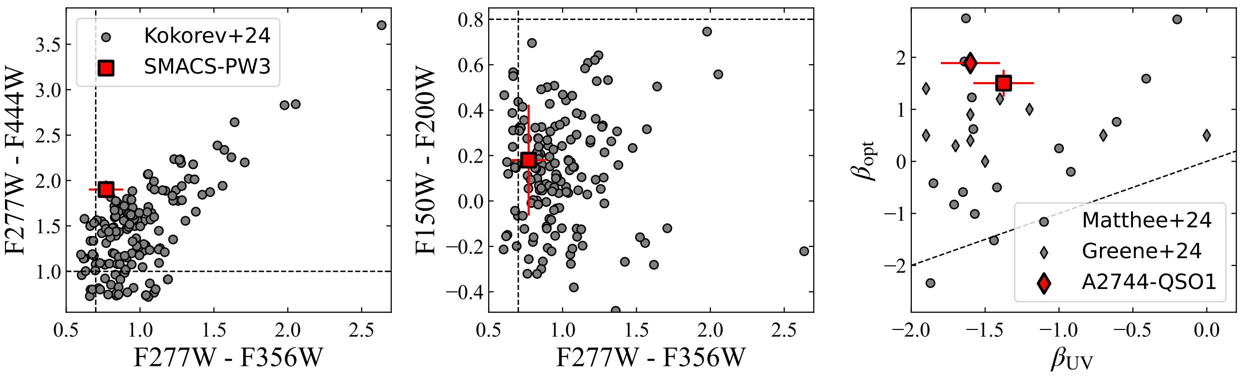

Fig. B.2. (Left and centre:) Color-color selection of LRDs utilising the selection criteria of Labbe et al. (2023) (indicated with dashed lines). The values we derive for PW3 (indicated by a square point) fall within all of the selection criteria. Examples of photometrically selected LRDs at z > 7 from Kokorev et al. (2024) are indicated (circular points). (Right:) The UV and optical slopes are assumed to be two independent power laws, after correcting F444W for the emission line flux seen in the grism spectra. Two notable z > 7 LRDs are indicated, both with very similar UV and optical slopes: PW3 from this work (red square) and QSO1 from Furtak et al. (2023) (red diamond). Spectroscopically confirmed LRDs at z = 4.2 − 5.5 (from Matthee et al. 2024, grey circles) and at z > 5 (from Greene et al. 2024, grey diamonds) are indicated. The black dashed line indicates where the UV and optical slopes are equal. We expect most LRDs to fall above this relation. It is clear that PW3 satisfies the LRD selection criteria and has typical UV and optical slopes for an LRD at z > 7.

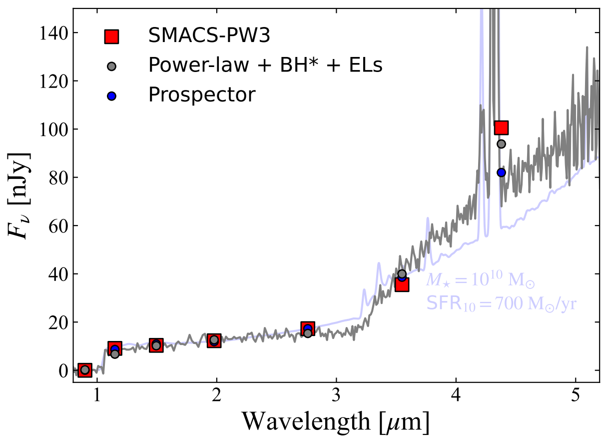

Fig. B.3. The photometry of the LRD candidate PW3 (red squares). We additionally show the best-fit `Prospector` model photometry (blue circles) and spectrum (blue solid line). Finally, we combine a power-law fit to the UV, with emission line constraints from the grism spectrum and the rescaled BH* spectrum from Naidu et al. (2025) to produce a combined spectrum (grey solid line) and photometry (grey circles). It is clear that our combined spectrum with the BH* reproduces the observed SED, while the `Prospector` model fails to match the rest-optical continuum.